Proceedings of the Canadian Society for Mechanical Engineering International Congress
32nd Annual Conference of the Computational Fluid Dynamics Society of Canada
Canadian Society of Rheology Symposium
CSME/CFDSC/CSR 2025
May 25–28, 2025, Montréal, Québec, Canada

DNS STUDY OF TURBULENT FLOWS IN A LARGE-AMPLITUDE WAVY-WALLED CHANNEL

Taylor C. Opperman and Bing-Chen Wang*

Department of Mechanical Engineering, University of Manitoba, Winnipeg, Canada
*BingChen.Wang@umanitoba.ca

***Abstract*—**Turbulent flow in a channel with a wavy bottom wall of varying Reynolds numbers ($Re_b = 5600$ and 9000) and a large wave amplitude-to-period ratio of $A/P = 0.4$ has been studied using direct numerical simulation (DNS). The Reynolds number effect on the turbulent flow has been thoroughly investigated through the analyses of the first- and second-order statistical moments of the velocity field. A separation region is observed in the wave troughs where the streamwise velocity is reduced and reversed, resulting in a region of augmented mean velocity and shear stresses. The TKE field is studied in physical space through mean contours and a budget balance of the TKE transport equation. Interestingly, unlike a smooth-channel flow, the turbulent production is shown to decrease with an increasing Reynolds number. The influence of Reynolds number on the TKE and turbulent production is further examined using the JPDF of the velocity fluctuations and pre-multiplied energy spectra.

***Keywords*—wavy-walled channel, direct numerical simulation, Reynolds number effect, turbulence**

I. Introduction

Wavy-channel flows have many practical engineering applications such as heat exchangers, boundary-layer modulation and preventing surface erosion [1, 2]. In the presence of a wavy wall, the symmetry about the midplane found commonly in a plane-channel flow no longer holds. Furthermore, the waves lead to increased momentum transfer in the bottom half of the channel as a result of the regions of flow separation and recirculation that are highly dependent on the amplitude-to-period ratio (A/P, also referred to as the wave steepness hereafter).

Buckles *et al.* [3] measured turbulent wavy-channel flow using laser Doppler velocimetry (LDV) at bulk Reynolds number 12000 to investigate flow separation under the influence of the wavy wall with $A/P = 0.2$. They identified three elements of the flow: a separated region, an attached boundary layer, and a free shear layer. A separation region was also seen by Hudson *et al.* [4] who conducted LDV experiments at a lower Reynolds number of $Re_b = 3380$ and a wave steepness of $A/P = 0.1$. Choi & Suzuki [5] used large eddy simulations (LES) and concluded that the near-wall streamwise vortex structures and the free shear layer had a drastic impact on the heat transfer in the lower half of the channel. They studied varying A/P values and concluded that heat transfer across the channel increased with wave steepness. Recently, Zhang *et al.* [6] performed LES to study scalar transport in a turbulent wavy-channel flow. They observed that the wavy wall increased turbulence kinetic energy (TKE) and drastically augmented the near wall flow structures.

Despite the previous contributions found in the literature, detailed DNS studies of turbulent wavy channel flows are still limited. Furthermore, the few available DNS studies have focused on walls with small wave steepness (defined as $A/P < 0.1$). In view of this knowledge gap, the goal of the current work is to conduct a comprehensive DNS study of the Reynolds number effects on large wave steepness (defined as $A/P > 0.1$) wavy-channel flow.

The current work is an extension of the previous work of Opperman *et al.* [7], which studied turbulent flow in a wavy channel with $A/P = 0.4$ at a fixed bulk Reynolds number of $Re_b = 5600$. The remainder of the paper is organized as follows. In Section II, the test case and numerical algorithm used to solve the governing equations are described along with a discussion of the domain size and mesh resolution and boundary conditions. In Section III, the DNS results are analyzed in detail using a variety of statistical methods. Finally, in Section IV, new research findings and major conclusions are summarized.

II. Test Cases and Numerical Algorithm

The continuity and momentum and equations that govern the incompressible flow are expressed as

$$\frac{\partial u_i}{\partial x_i} = 0 \quad , \tag{1}$$

and

$$\frac{\partial u_i}{\partial t} + u_j \frac{\partial u_i}{\partial x_j} = -\delta_{1i} \frac{\Pi}{\rho} - \frac{1}{\rho} \frac{\partial p}{\partial x_i} + \nu \frac{\partial^2 u_i}{\partial x_j^2} \quad , \tag{2}$$

respectively. Here, u_i, ρ, ν, δ_{1i} and p are the velocity, density, viscosity, Kronecker delta and pressure of the flow field, respectively. Tensor notation is used, and the coordinates

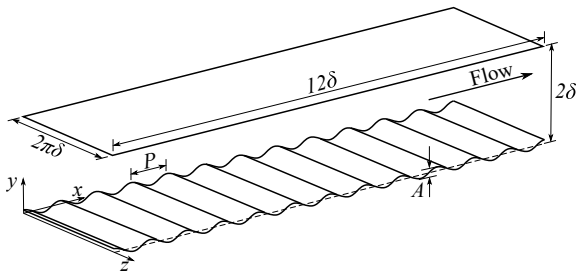

Figure. 1: Schematic diagram of a wavy-walled channel.

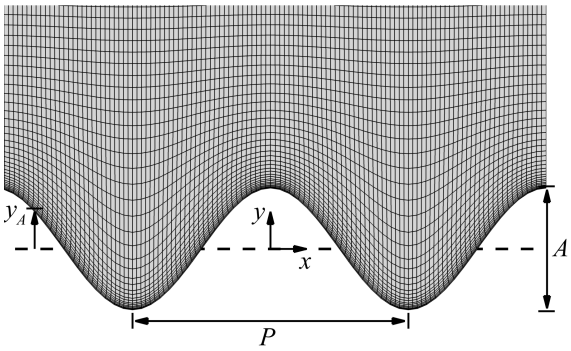

Figure. 2: Partial mesh of a wavy-walled channel. For clarity, only 2 of the 12 wave periods and one in every 4 grid points are shown.

(x, y, z) and velocities (u, v, w) correspond to (x_1, x_2, x_3) and (u_1, u_2, u_3), respectively. The flow is driven in the streamwise direction by a constant mean pressure gradient Π. The flow is fully developed and periodic boundary conditions are applied to the streamwise and spanwise directions. In addition, a no-slip boundary condition is enforced at both walls. Two test cases ($WC1$ and $WC2$ with $Re_b = 5600$ and 9000, respectively) of the wavy-channel flows are considered in our comparative study to investigate the effects of Reynolds number. Both cases have a fixed wave steepness of $A/P = 0.4$. As shown in Fig. 1, the domain has a length of $L_x = 12\delta$, a width of $L_z = 2\pi\delta$ and a height of $L_y = 2\delta$ for both wavy-walled cases, where δ is the channel half height. The wavy wall is centered about its midplane ($y/\delta = 0$) and its geometry is defined by $y_A = y_A(x) = \frac{A}{2}\cos\left(\frac{2\pi x}{P}\right)$. The wave period is held constant at $P = \delta$. In order to identify the wave effects, two smooth-channel flows ($SC1$ and $SC2$ with $Re_b = 5600$ and 9000, respectively) were simulated for the purpose of comparison, with dimensions of $L_x \times L_y \times L_z = 4\pi\delta \times 2\delta \times 2\pi\delta$.

The bulk Reynolds number is defined as $Re_b = U_b\delta/\nu$ for all four cases, where U_b is the bulk mean velocity based on the average channel height 2δ. Alternatively, the Reynolds number can also be defined using the wavy-wall friction velocity as $Re_{\tau w} = \frac{u_{\tau w}\delta}{\nu} = 316$ and 556 for cases $WC1$ and $WC2$, respectively, where the subscript 'w' denotes values at the wavy wall. The friction velocity is defined similar to that used by Ismail *et al.* [8] (i.e., $u_\tau^2 = D_p + D_v$) where the form and viscous drag are given by

$$D_p = \frac{1}{\rho L_x}\int_{\partial\Omega}\langle p\rangle\, dy \quad , \tag{3}$$

and

$$D_\nu = \frac{\nu}{L_x}\int_{\partial\Omega}\left[\left(\frac{\partial\langle u\rangle}{\partial y} + \frac{\partial\langle v\rangle}{\partial x}\right)dx - 2\frac{\partial\langle u\rangle}{\partial x}dy\right] \quad , \tag{4}$$

respectively. In these equations '$\partial\Omega$' denotes the boundary of either the smooth top, or the wavy bottom wall.

The governing equations are solved using a spectral-element code developed by Blackburn *et al.* [9], which has a spectral accuracy and is highly suitable for conducting DNS in a rigorous manner. The code is written in the coding language C++, calls to routines that are written in FORTRAN and C, and is made parallel using message passing interface (MPI) libraries. The x-y plane is divided into 14400 quadrilateral elements and a 4th-order Guass-Labatto-Legendre Lagrange (GLLL) polynomial is used for the further spatial discretization of each finite element. The spectral element mesh is then expanded into 240 Fourier modes in the z-direction for both wavy-channel cases, and thus, the domain contains approximately 55 million grid points ($1440 \times 161 \times 240$). The wavy-channel mesh is shown in Fig. 2 for the bottom half of the channel for two periods. Only every 4th grid point is plotted for clarity in Fig. 2. In other words, the coarse mesh is displayed before the GLLL polynomial discretization is applied. All physical quantities are expanded into 240 Fourier modes in the z-direction for all of the wavy channel flows. The grid spacing in the z-direction is uniform and the spacing in the x- and y-directions are refined to ensure a precise calculation of the wall shear. A summary of the grid resolutions are given in Tab. I, in which Δy^+_{max}, Δx^+_{max}, and Δz^+ are values taken at the first node away from the wall and $(\Delta/\eta)_{max}$ is the maximum ratio of the grid resolution to the Kolmogorov length scale of the entire domain. In the analysis, the instantaneous velocity is decomposed as $u = \langle u\rangle + u'$, where $\langle\cdot\rangle$ represents variables averaged over time and homogeneous spatial directions, and $(\cdot)'$ represents fluctuations from the mean. Variables expressed in wall coordinates denoted by superscript '+' were obtained using the average of the top and bottom wall friction velocity $u_{\tau A}$. Additionally, a relative streamwise coordinate x' is defined within an arbitrary wave period (peak to peak), starting from the upstream wave peak (where $x' = 0$) and ending at the downstream peak (where $x' = \delta$). All averaging was done over 600 instantaneous flow fields that were collected over at least 30 large eddy turn over times (LETOT, defined as $\delta/u_{\tau A}$) once the flow became fully developed and statistically stationary after a precursor simulation. Simulations and data storage were executed on the Grex supercomputer located at the University of Manitoba.

TABLE. I: Summary of the grid resolutions of each wavy-channel test case.

Case	$\mathbf{N_x \times N_y \times N_z}$	$\mathbf{\Delta y^+_{max}}$	$\mathbf{\Delta x^+_{max}}$	$\mathbf{\Delta z^+}$	$\mathbf{(\Delta/\eta)_{max}}$
$WC1$	1440×161×240	0.25	3.45	8.28	3.05
$WC2$	1440×161×240	0.45	6.06	14.55	4.29

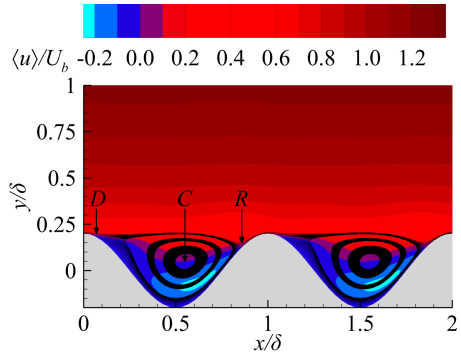

(a) Case $WC1$

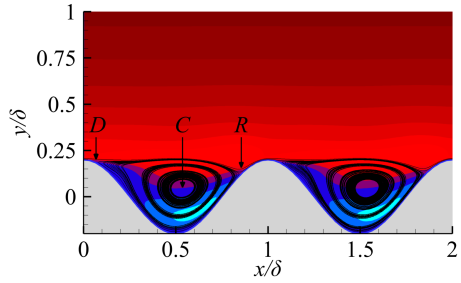

(b) Case $WC2$

Figure. 3: Contour plots of the non-dimensional mean streamwise velocity $\langle u \rangle / U_b$ shown for two arbitrary periods of the domain superimposed with the mean streamlines. Letters 'D', 'C' and 'R' denote the mean flow detachment, recirculation center and reattachment points, respectively.

III. Results and Discussion

Figs. 3(a) and (b) present the contours of the mean streamwise velocity (non-dimensionalized by U_b) for case $WC1$ and $WC2$, respectively. Only the lower half of the channel is shown for the sake of clarity. Letters 'D', 'C' and 'R' indicate the points of flow detachment, recirculation center and flow reattachment, respectively. As shown in Fig. 3, the mean flow detaches from the leeward side of the wave peak (point D) at $x'/\delta = 0.068$ and 0.050 for $WC1$ and $WC2$, respectively. The point of the mean flow reattachment on the windward side of the wave peak (point R) occurs at $x'/\delta = 0.860$ to 0.851 for cases $WC1$ and $WC2$, respectively. The center of the recirculation center (point C) shifts slightly from $(x'/\delta, y/\delta)$=$(0.551,\ 0.051)$ to $(0.537,\ 0.047)$ as the Reynolds number increases from case $WC1$ to $WC2$. From this, two trends can be observed in the separation region as the Reynolds number increases. Firstly, the length of the separation region (i.e., the distance between points D and R) clearly increases in size from case $WC1$ to $WC2$. Secondly, the separation region as a whole shifts upstream slightly within a wave period from case $WC1$ to $WC2$.

Fig. 4 compares the profiles of the non-dimensional streamwise velocity $\langle u \rangle / U_b$ at the wave peak ($x'/\delta = 0.0$) and dip ($x'/\delta = 0.5$) locations. The vertical purple line in Fig. 4(b) denotes the height of the wave peak ($y/\delta = 0.2$) for the two wavy-channel test cases. In contrast to the smooth-channel flow cases, the vertical profiles of $\langle u \rangle / U_b$ for the wavy-channel flow cases are asymmetrical about the channel center.

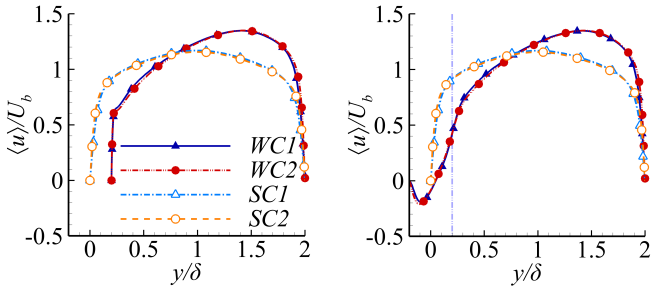

(a) Peak location (b) Dip location

Figure. 4: Vertical profiles of the non-dimensional mean streamwise velocity $\langle u \rangle / U_b$ at the wave peak and dip locations. The vertical purple line in panel (b) denotes the height of the wave peak ($y/\delta = 0.2$).

The vertical position of peak $\langle u \rangle / U_b$ is pushed towards the smooth wall with the addition of the wavy wall. Furthermore, the vertical position of peak $\langle u \rangle / U_b$ shifts upwards from $y/\delta = 1.41$ to 1.43 as the Reynolds number increases from case $WC1$ to $WC2$. Clearly, the vertical profiles of the streamwise velocity are much more complex at the wave dip location compared to the wave peak location. By comparing Figs. 4(a) and (b), it can be seen that the profiles of $\langle u \rangle / U_b$ for a given test case are similar at both the wave peak and dip locations in the upper half of the channel. Clearly, the influence of the wavy wall diminishes as the smooth wall is approached. This is consistent with the observations of the velocity contours in Fig. 3, which showed that $\langle u \rangle / U_b$ quickly becomes insensitive to the streamwise coordinate (x) away from the wavy wall.

The vertical profiles of the non-dimensional Reynolds $(-\langle u'v' \rangle / U_b^2)$ and viscous $(\langle \tau_{12} \rangle / \rho U_b^2)$ shear stresses are presented in Figs. 5(a) and (b), respectively, at the wave dip location ($x'/\delta = 0.5$). The vertical purple lines denote the height of the wave peak ($y/\delta = 0.2$) for the two wavy-channel test cases. From Fig. 5(a), it can be seen that the Reynolds shear stress is dramatically enhanced in the wavy-channel flows compared to the smooth-channel flows. It is interesting to observe that the profiles of $-\langle u'v' \rangle$ are very similar between cases $WC1$ and $WC2$. From Fig. 5(b), it is seen that the viscous shear stress is highly augmented for the wavy-channel flows compared to the smooth-channel flows. In particular, the profiles are nearly zero at the lower wall (rather than reaching a maximum as is the case for a smooth channel flow) due to the dampened flow inside the recirculation region. Additionally, $\langle \tau_{12} \rangle$ reaches a local maximum at the height of the wave peak for both wavy-channel test cases as a result of the free shear layer induced by the wavy surface. Interestingly, the local peak in viscous shear stress decreases with increases in Reynolds number. This may be explained by the enhanced transport of momentum into the upper half of the channel, resulting in decreases in the velocity gradient $\partial \langle u \rangle / \partial y$ in the lower half of the channel as Reynolds number increases. This explanation is supported by the mean velocity profiles shown in Fig. 4.

Figs. 6(a)-(c) show the vertical profiles of the root mean

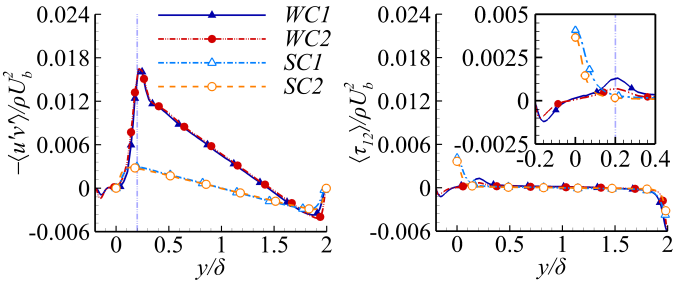

(a) Reynolds shear stress (b) Viscous shear stress

Figure. 5: Vertical profiles of the non-dimensional Reynolds ($-\langle u'v'\rangle/U_b^2$) and viscous ($\langle\tau_{12}\rangle/\rho U_b^2$) shear stresses at the wave dip location. The vertical purple lines denote the height of the wave peak ($y/\delta = 0.2$).

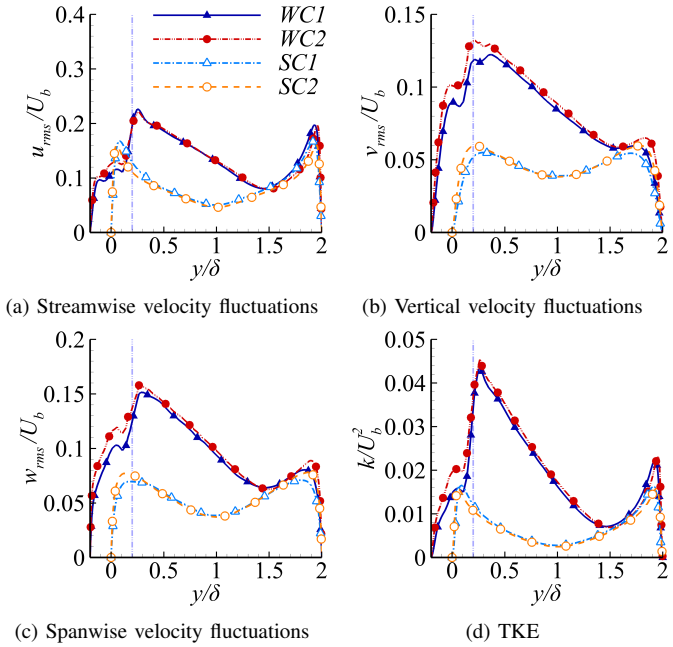

(a) Streamwise velocity fluctuations (b) Vertical velocity fluctuations

(c) Spanwise velocity fluctuations (d) TKE

Figure. 6: Vertical profiles of the RMS velocities u_{rms}, v_{rms} and w_{rms} (non-dimensionalized by U_b), and the TKE k (non-dimensionalized by U_b^2) at the wave dip location. The vertical purple lines denote the height of the wave peak ($y/\delta = 0.2$).

square (RMS) velocity fluctuations (non-dimensionalized using U_b) and Fig. 6(d) presents the vertical profiles of the TKE (non-dimensionalized using U_b^2) all at the wave dip location. The vertical purple lines in Fig. 6 denotes the height of the wave peak ($y/\delta = 0.2$) for the two wavy-channel test cases. A careful comparison of Figs. 6(a)-(c) reveals that u_{rms} is fairly insensitive to increases in Reynolds number for the two wavy-channel test cases, particularly above the height of the wave peak. In contrast, the magnitudes of v_{rms} and w_{rms} increase as the Reynolds number increases. Referencing Fig. 6(d), it is understood that as the Reynolds number increases, any enhancement in the TKE is the result of enhanced vertical and spanwise turbulent velocity fluctuations.

Fig. 7 compares the TKE contours (non-dimensionalized by U_b^2) of the two Reynolds numbers tested. It is evident that the turbulent motions are strengthened dramatically near the wavy wall, and the magnitude of TKE increases with an increasing

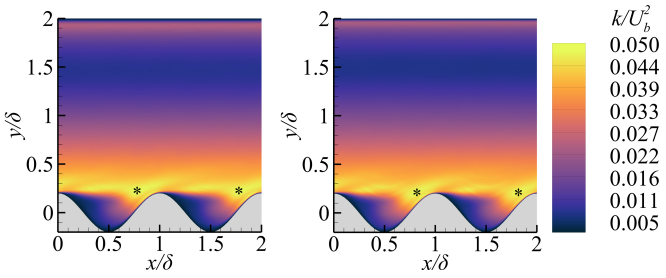

(a) Case $WC1$ (b) Case $WC2$

Figure. 7: Contours of the non-dimensional TKE k/U_b^2 shown for two periods of the domain for the two Reynolds numbers tested. The black '$*$' symbol indicates the maximum value of k/U_b^2.

value of A/P. As shown in Fig. 7, the distribution of TKE in a wavy-channel flow is affected significantly by the free shear layer induced by the waves and the flow impingement on the windward side of the waves. It is seen that the location of the TKE peak (marked with the black '$*$' symbol in Fig. 7) is slightly above the wave peak at $x'/\delta, y/\delta = (0.791,\ 0.224)$ and $(0.817,\ 0.215)$ for cases $WC1$ and $WC2$, respectively. Clearly, the location of peak TKE shifts further downstream and closer to the wall as the Reynolds number increases.

To develop a deeper understanding of the Reynolds number effects on the TKE, its transport equation can be studied. In a statistically-stationary incompressible flow, it is expressed as

$$\underbrace{-\frac{1}{2}\langle u_j\rangle\frac{\partial\langle u_i'u_i'\rangle}{\partial x_j}}_{H_k}\underbrace{-\langle u_i'u_j'\rangle\frac{\partial\langle u_i\rangle}{\partial x_j}}_{P_k}\underbrace{+\frac{1}{\rho}\langle p's_{ii}'\rangle}_{\Pi_k=0}\underbrace{-\frac{1}{2}\frac{\partial\langle u_i'u_i'u_j'\rangle}{\partial x_j}}_{D_k^t}$$
$$\underbrace{-\frac{1}{\rho}\frac{\partial\langle p'u_j'\rangle}{\partial x_j}}_{D_k^p}\underbrace{+\frac{\nu}{2}\frac{\partial^2\langle u_i'u_i'\rangle}{\partial x_j\partial x_j}}_{D_k^v}\underbrace{-\nu\left\langle\frac{\partial u_i'}{\partial x_j}\frac{\partial u_i'}{\partial x_j}\right\rangle}_{\varepsilon_k}=0\quad, \tag{5}$$

where H_k, P_k, Π_k and ε_k are the convection, production, pressure-strain and viscous dissipation terms, respectively. The TKE diffusion is broken up into the turbulent, pressure and viscous components, denoted by D_k^t, D_k^p and D_k^v, respectively.

Fig. 8 compares the vertical profiles of the TKE budget terms (non-dimensionalized using U_b^3/δ) of the two wavy-channel test cases ($WC1$ and $WC2$) at the wave dip location ($x'/\delta = 0.5$) against those of the smooth-channel test cases ($SC1$ and $SC2$). For all of the cases studied, the budget balance of TKE is dominated by viscous-dissipation ε_k and viscous-diffusion D_k^v in the near-wall region. As $y/\delta = 1.0$ is approached, the magnitudes of the budget terms diminish and the balance is primarily between P_k and ε_k. The profiles of the TKE budget terms at the location of the wave dip for cases $WC1$ and $WC2$ are presented in Figs. 8(c) and (d), respectively. By comparing Figs. 8(c) and (d) with the smooth channels in 8(a) and (b), it is apparent that the budget balances of the wavy-walled cases exhibit more complex profiles than those of the smooth-channel cases, specifically around the wave peak height (at $y/\delta = 0.2$). The most significant contrast in the budget balance of TKE between wavy-channel and the smooth-channel is the enhanced convection term H_k around

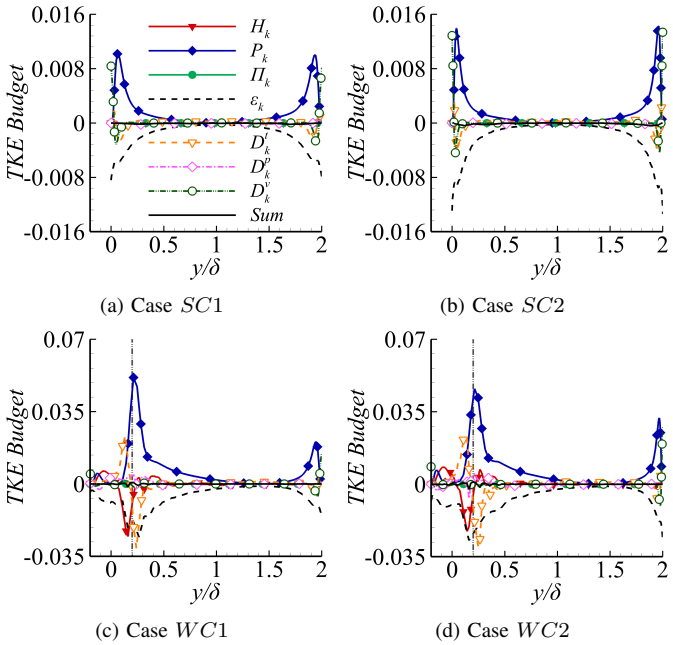

(a) Case $SC1$ (b) Case $SC2$

(c) Case $WC1$ (d) Case $WC2$

Figure. 8: Vertical profiles of the TKE budget terms non-dimensionalized using U_b^3/δ at the wave dip location. The vertical gray dashed line denotes the height of the wave peak ($y/\delta = 0.2$).

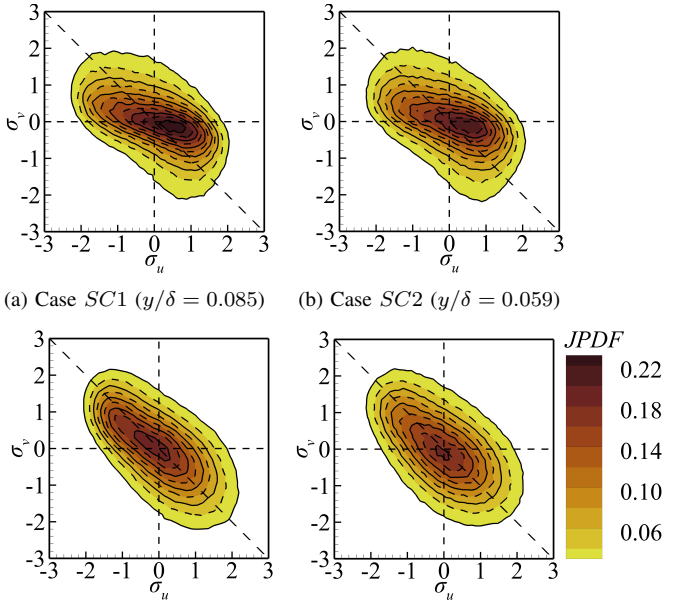

(a) Case $SC1$ ($y/\delta = 0.085$) (b) Case $SC2$ ($y/\delta = 0.059$)

(c) Case $WC1$ ($y/\delta = 0.250$) (d) Case $WC2$ ($y/\delta = 0.265$)

Figure. 9: Contours of JPDF of u'/u_{rms} and v'/v_{rms} at the height of maximum TKE for all four test cases.

the height of the wave peak, where strong shear flows are induced which generate flow inhomogeneity in both the x- and y-directions. The profiles of cases $WC1$ and $WC2$ are qualitatively similar as the convection term attains a small positive peak near the wavy wall (below $y/\delta = 0.0$), acting as a local source term of TKE and carrying high TKE fluid down into the wave dip. However, immediately above the midpoint of the wave, the convection term H_k attains a large negatively-valued peak, acting as one of the dominant sink terms of TKE to carry high TKE fluid away from the energy-producing free shear layer. At this position, the turbulent diffusion and viscous-dissipation (i.e., D_k^t and ε_k, respectively) are the two main sink terms, both reaching negatively-valued peaks. As the value of the Reynolds number increases, the peak magnitudes of H_k and D_k^t increase monotonically. As such, the stronger convection and turbulent diffusion of TKE away from the energy-producing shear layer results in a larger region of strong TKE. The turbulent production term P_k is balanced primarily by these three sink terms of H_k, D_k^t and ε_k in this region between the wave center and the wave peak. It is interesting to observe that opposite to the trends of the smooth-channel flows, the magnitude of the peak turbulent production decreases in the wavy-channel flows as the Reynolds number increases. However, a careful examination of Fig. 8 reveals that the profiles of the TKE budget terms near the upper smooth wall are qualitatively similar and exhibit similar trends with respect to increases in Reynolds number.

A key component to the turbulent production of TKE is the Reynolds shear stress $-\langle u'v' \rangle$. To further understand the effects of Reynolds number on $-\langle u'v' \rangle$, the JPDF of non-dimensionalized instantaneous velocity fluctuations $\sigma_u = u'/u_{rms}$ and $\sigma_v = v'/v_{rms}$ is calculated. The JPDF for the wavy-channel test cases are assessed at the streamwise location of the wave dip ($x'/\delta = 0.5$) for all vertical elevations. In Fig. 9, the JPDF of σ_u and σ_v for each wavy-channel flow case is compared to those of the smooth-channel flow cases at the vertical height of maximum TKE (i.e., $y/\delta = 0.085$, 0.059, 0.250 and 0.265 for cases $SC1$, $SC2$, $WC1$ and $WC2$, respectively). Fig. 9 shows that the streamwise and vertical velocity fluctuations synchronize well with each other for all flow cases, as the JPDF plots are aligned along 135° through quadrant two ($Q2$) and quadrant four ($Q4$) denoted by a diagonal dashed line. It is observed that the alignment is more pronounced in the wavy-walled test cases compared to the smooth-channel test cases. This alignment preference is a well-known conclusion of the classical boundary layer theory, giving rise to positively-valued Reynolds stress $-\langle u'v' \rangle$ near the wall due to the dominance of these ejection and sweep events [10]. Fig. 9(c) and (d) shows that the largest values of the JPDF become more concentrated at the origin for case $WC2$ compared to $WC1$, indicating that the magnitudes of the most common velocity fluctuations decrease with increases in Reynolds number. These results are supported by the findings of Figs. 8(c) and (d), which show that TKE production decreases at this location with increases in Reynolds number.

Thus far, the analysis has been conducted in the physical space. To refine the study, it is useful to examine the pre-multiplied energy spectrum, $k_z E_k$, where k_z is the wave number in the spanwise direction and $E_k = 0.5 \langle \widehat{u_i'}^* \widehat{u_i'} \rangle$ is the spanwise energy spectrum. Here, a hat $\widehat{(\cdot)}$ denotes the Fourier transform of an arbitrary flow variable, and a superscript $(\cdot)^*$ denotes the conjugate part of a complex number. Fig. 10 compares the isopleths of the non-dimensional

spanwise pre-multiplied energy spectra $\delta k_z E_k/U_b^2$ for all four test cases, plotted with respect to the non-dimensional spanwise wavelength ($\lambda_z = 2\pi/k_z$) along the vertical line going through the wave dip ($x'/\delta = 0.5$). In Fig. 10, the peak position of the non-dimensional pre-multiplied energy spectrum (or, max($\delta k_z E_k/U_b^2$)) is labeled using the yellow '$*$ symbol, while the red dashed line delineates the height of the wave peak ($y/\delta = 0.2$). Three energy levels are distinguished, and the innermost, intermediate, and outermost isopleths correspond to 5/8-th, 1/4-th, and 1/8-th of the peak value (or, $0.625\text{max}(\delta k_z E_k/U_b^2)$, $0.25\text{max}(\delta k_z E_k/U_b^2)$, and $0.125\text{max}(\delta k_z E_k/U_b^2)$). The high-intensity core enclosed by the innermost isopleth of $0.625\text{max}(\delta k_z E_k/U_b^2)$ corresponds to the most energetic eddies of the turbulent flow field of a narrow range of wavelengths. By contrast, the low-intensity core enclosed by the outermost isopleth $0.125\text{max}(\delta k_z E_k/U_b^2)$ corresponds to much less energetic eddies encompassing a larger range of wavelengths. Clearly, the outermost isopleth has been fully captured in all test cases, indicating that the spanwise size of the domain is sufficiently large such that not only high-intensity but also low-intensity turbulent motions have been well captured in our DNS.

The peak value (or, mode) of $\delta k_z E_k/U_b^2$ occurs at (λ_z/δ, y/δ) = (0.626, 0.100), (0.452, 0.058), (0.699, 0.275) and (0.483, 0.252) near the lower channel wall for cases $SC1$, $SC2$, $WC1$ and $WC2$, respectively. Clearly, as the Reynolds number increases (from case $WC1$ to $WC2$), the non-dimensional characteristic wavelength (corresponding to the modal value of λ_z/δ) decreases. It is also observed that the maximum value of $\delta k_z E_k/U_b^2$ near the wavy wall occurs just above the height of the wave peak for both Reynolds number test cases, which indicates that the most energetic vortex cores are concentrated around the height of the free shear layer induced by the wave crest. This agrees well with the previous analysis of Figs. 7 and 8 where elevated levels of TKE and rates of TKE production are observed in the free shear layer.

IV. Conclusion

Turbulent flows and structures in a wavy channel of varying Reynolds numbers and a fixed large wave amplitude-to-period ratio have been studied using DNS. Additionally, two plane-channel flows of the same bulk Reynolds numbers were simulated as baseline cases for comparison. The TKE in the wavy-channel flow is seen to increase as the Reynolds number increases. Interestingly, the RMS velocity components show increases in the overall TKE as Reynolds number increases are attributed to enhancements in the vertical and spanwise velocity fluctuations rather than those of the streamwise velocity fluctuations. Furthermore, at the location of the wave dip, profiles of the TKE transport budget terms reveal that the peak turbulent production does not always increase with Reynolds number, as is the case in a smooth-channel flow. The plots of the 1-D pre-multiplied energy spectra $\delta k_z E_k/U_b^2$ concluded that as the Reynolds number increases, the characteristic length of the energetically relevant turbulent motions decreases.

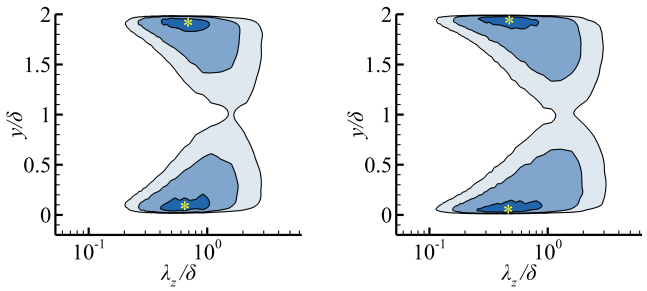

(a) Case $SC1$ (b) Case $SC2$

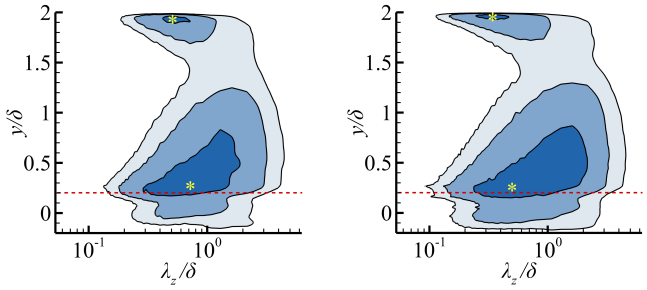

(c) Case $WC1$ (d) Case $WC2$

Figure. 10: Isopleths of the non-dimensional pre-multiplied 1-D energy spectrum $\delta k_z E_k/U_b^2$, displayed with respect to the non-dimensional spanwise wavelength λ_z/δ and vertical direction y/δ extracted at $x'/\delta = 0.5$ for cases $WC1$ and $WC2$ in panels (c) and (d). The yellow '$*$ symbol indicates the peak value of $\delta k_z E_k/U_b^2$. Three contour levels of energy spectrum are plotted, and the innermost, intermediate and outermost isopleths correspond to 62.5%, 25% and 12.5% of the peak value, respectively. The red dashed line indicates the height of the wave peak ($y/\delta = 0.2$).

Acknowledgment

The authors would like to thank the University of Manitoba for access to the GREX supercomputing and storage facilities.

References

[1] B. Poulson, "Predicting and preventing flow accelerated corrosion in nuclear power plant," Int. J. Nucl. Energy, vol. 2014, pp. 1–23, 2014.

[2] D. Borello, D. Anielli and F. Rispoli "Unsteady CFD analysis of erosion mechanism in the coolant channels of a rotating gas turbine blade.," In the proceedings of ASME Turbo Expo 2015: Power of Land, Sea and Air, Montreal, Canada, vol. 5A:2015, p. V05AT11A028, 2015.

[3] J. Buckles, T. J. Hanratty and R. J. Adrian "Turbulent flow over large-amplitude wavy surfaces," J. Fluid Mech., vol. 140 , pp. 27–44, 1984.

[4] J. D. Hudson, L. Dykhno and T. J Hanratty "Turbulence production in flow over a wavy wall," Exp. Fluids, vol. 20 , pp. 257–265, 1996.

[5] H. S. Choi and K. Suzuki "Large eddy simulation of turbulent flow and heat transfer in a channel with one wavy wall," Int. J. Heat Fluid Flow, vol. 26 , pp. 681–694, 2005.

[6] E. Zhang, X. Wang and Q. Liu, "Effects of spanwise heterogeneity of a three-dimensional wavy wall on momentum and scalar transport," Phys. Fluids, **33**(5), 055116, 2021.

[7] T. Opperman, W. J. Xiong and B. C. Wang "DNS study of turbulent flow in a channel with a wavy bottom wall," In the proceedings of the 10^{th} International Symposium on Turbulence Heat and Mass Transfer, Rome, Italy, vol. E026 , pp. 185–188, September 2023.

[8] U. Ismail, T. A. Zaki and P. A. Durbin "Simulations of rib-roughened rough-to-smooth turbulent channel flow," J. Fluid Mech., vol. 843 , pp. 419–449, 2008.

[9] H. M. Blackburn, D. Lee, T. Albrecht and J. Singh "Semtex: a spectral element Fourier solver for the incompressible Navier-Stokes equations in cylindrical or Cartesian coordinates," Comput. Phys. Commun., vol. 57(106804), 2019.

[10] R. J. Adrian "Hairpin vortex organization in wall turbulence," Phys. Fluids, **19**(4), 041301, 2007.